Energies **2015**, *8*, 4920-4942; doi:10.3390/en8064920

OPEN ACCESS

energies

ISSN 1996-1073

www.mdpi.com/journal/energies

Article

Magnetic Field Equivalent Current Analysis-Based Radial Force Control for Bearingless Permanent Magnet Synchronous Motors

Huangqiu Zhu and Hui Li *

School of Electrical and Information Engineering, Jiangsu University, Zhenjiang 212013, China; E-Mail: zhuhuangqiu@ujs.edu.cn

* Author to whom correspondence should be addressed; E-Mail: lihui090232@163.com; Tel.: +86-157-5101-0795; Fax: +86-511-8878-0088.

Academic Editor: Enrico Sciubba

Received: 22 December 2014 / Accepted: 22 May 2015 / Published: 27 May 2015

Abstract: Bearingless permanent magnet synchronous motors (BPMSMs), with all advantages of permanent magnet motors (PMSMs) and magnetic bearings, have become an important research direction in the bearingless motor field. To realize a stable suspension for the BPMSM, accurate decoupling control between the electromagnetic torque and radial suspension force is indispensable. In this paper, a concise and reliable analysis method based on a magnetic field equivalent current is presented. By this analysis method, the operation principle is analyzed theoretically, and the necessary conditions to produce a stable radial suspension force are confirmed. In addition, mathematical models of the torque and radial suspension force are established which is verified by the finite element analysis (FEA) software ANSYS. Finally, an experimental prototype of a 2-4 poles surface-mounted BPMSM is tested with the customized control strategy. The simulation and experimental results have shown that the motor has good rotation and suspension performance, and validated the accuracy of the proposed analysis method and the feasibility of the control strategy.

Keywords: bearingless permanent magnet synchronous motor; magnetic field equivalent current; decoupling control; radial suspension force

1. Introduction

Bearingless motors combine the characteristics of conventional motors and magnetic bearings. Compared with magnetic bearings, bearingless motors possess the advantages of shorter shaft length, higher critical speed, and lower cost [1]. Among different types of bearingless motors, bearingless permanent magnet synchronous motors (BPMSMs) are highly valued around the world due to their virtues of small size, light weight, non-contact, no wear, no lubrication, high efficiency, high power factor, and so on [2]. They have broad application prospects in centrifugal machines, aeronautics and astronautics, life science, *etc.* Especially due to their non-contact and no lubrication characteristics, BPMSMs are employed successfully in high purity environments, such as the semiconductor, pharmaceutical and medical industries.

Until now, the advanced technologies of the BPMSMs, including mathematical models, motor topologies and control strategies, have been investigated and discussed extensively by researchers. The complete mathematical models of the surface mounted BPMSMs are studied in [3] by using the Maxwell stress tensor method, which can effectively compensate for the effect of rotor eccentricity and Lorentz force. In [4], a new modeling method based on mechanical to electrical coordinate transformation is put forward, which proves an effective modeling method. For the motor topologies, Ooshima proposed a rotor design method considering demagnetization for a 2-DOF BPMSM [5]. Besides, a 5-DOF BPMSM, consisting of a 3-DOF axial-radial magnetic bearing and a 2-DOF BPMSM, is presented in [6]. At the same time, Kascak provided another novel 5-DOF BPMSM, only consisting of two conical BPMSMs to realize the 5-DOF active control [7]. For the control strategies, the decoupling control algorithm based on the rotor flux orientation control (FOC) has been widely used in recent decades [4]. The direct radial displacement control strategy, based on the relationship between the rotor radial displacement and radial suspension force, is pointed out in [8]. In addition, many artificial-intelligence-based control strategies to effectively handle the nonlinearities of the BPMSM system are also presented, such as sliding mode variable structure control [9], artificial neural network inverse control [10] and genetic algorithm control.

The double-winding BPMSM has two sets of coupling windings in the stator slot, namely torque windings (pole pair is P_M) and suspension force windings (pole pair is P_B). Thus, the precise decoupling control between them is indispensable to realize the suspension operation. In [11], by marking the distribution situation of the torque winding flux linkage and suspension force winding flux linkage, the generation principle of radial suspension forces is studied. Then, the corresponding performance of the induction type bearingless motor can be verified by the 2D finite element analysis (FEA) model. Based on these methods, analyses of the bearingless motor suspension characteristics have become simple, direct and operable. However, as the calculated coefficients are hard to get, the mathematical models are inaccurate. In [12], the mathematical model of the surface-mounted BPMSM is established based on the principle of virtual displacement. The derived idea is as follows: firstly, according to the equivalent magnetic circuit principle, the inductance matrixes are deduced. Then the expressions of electromagnetic energy based on inductance matrixes are derived. Finally, the mathematical expressions of radial suspension forces can be deduced by partial derivation with respect to the electromagnetic energy expressions. This method makes the deduction of radial suspension forces easier and more visual. The inductance parameters, however, are difficult to obtain precisely

through experimental measurements, therefore, the precise calculation of radial suspension force also cannot be achieved for the BPMSM.

In this paper, an accurate and reliable analysis method based on the magnetic field equivalent current is presented. Based on this analysis method, the practical motor windings are replaced by equivalent windings existing in different material spaces. Distributions of these equivalent windings only depend on air gap magnetic fields, and they are not subject to the mechanical structure features. Then, the interactions among the air gap magnetic fields can be converted to that of the carrying-current equivalent windings. Thus, some complex analyses of magnetic fields can be avoided and the difficulty of system analysis can be effectively reduced, which provides a systemic theoretical foundation for the control of radial suspension forces.

2. Magnetic Field Equivalent Current-Based Analysis of Radial Suspension Forces

2.1. Fundamental Theory of the Magnetic Field Equivalent Current Analysis Method

Assuming that the motor windings are designed as spatially symmetric distributions, the permeability in the air gap is equal everywhere, the leakage inductances of permanent magnets and magnetic saturation are ignored. The air gap magnetic fields are thought to be produced by a series of carrying-current equivalent windings. The pole pairs of equivalent windings are equal to that of the original air gap magnetic fields. The distributions of the equivalent windings are flexibly designed according to the actual air gap magnetic fields. The equivalent full pitch windings are employed in this paper and they can rotate with the change of the air gap magnetic fields. The current in equivalent windings is considered as direct current. Then, the interaction relationships between torque winding air gap magnetic field and suspension force winding air gap magnetic field can be obtained indirectly from that of the corresponding equivalent currents. Figure 1 shows the schematics of magnetic field equivalent current analysis method.

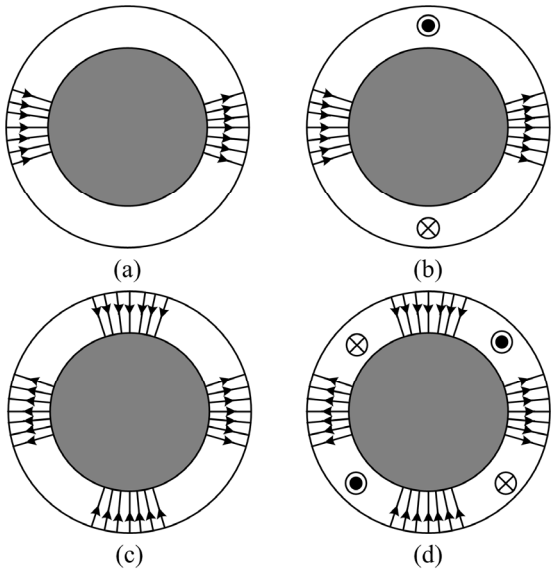

Figure 1. Schematic diagrams of magnetic field equivalent current analysis method. (**a**) 2-pole air gap magnetic field; (**b**) Equivalent winding currents of 2-pole air gap magnetic field; (**c**) 4-pole air gap magnetic field; (**d**) Equivalent winding currents of 4-pole air gap magnetic field.

In this paper, the analysis method based on carrying-current equivalent windings is defined as the magnetic field equivalent current analysis method. The equivalent windings produced by the torque winding air gap magnetic field are defined as the equivalent torque windings, and the equivalent windings generated by the suspension force winding air gap magnetic field are defined as the equivalent suspension force windings. In addition, on the basis of field distributions, many structural forms can be composed of equivalent torque windings and equivalent suspension force windings. Among them, intensifying factor and softening factor are two key structural forms, as shown in Figure 2. The upper layer of windings corresponds to equivalent suspension force windings, while the lower layer of windings corresponds to equivalent torque windings. Intensifying factor and softening factor are formed by two sets of equivalent windings with their centre line overlapped. The enhanced resultant air gap magnetic fields can be produced by the intensifying factor, and the maximum magnetic motive force (MMF) can be formed. The reduced resultant air gap magnetic fields can be produced by the softening factor, and the minimum MMF can be generated. If the centre lines of the two sets of equivalent windings are no longer overlapped, but there exists an inclusion relation in space, the magnetic field superposition effect between windings is the same as that of intensifying factor and softening factor. Then, these structure forms are defined as partial-intensifying factor and partial-softening factor.

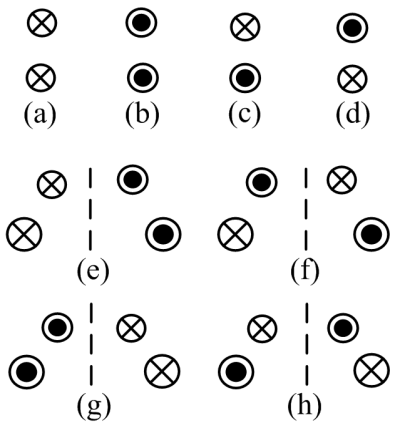

Figure 2. Basic current structure formed by two sets of windings. (**a**), (**b**), (**e**) and (**g**) are intensifying factors. (**c**), (**d**), (**f**) and (**h**) are softening factors.

2.2. The Principle of Radial Suspension Force Generation for the BPMSM

Figure 3 shows the stator configuration and the 2D FEA model of a surface-mounted BPMSM. To orientate and start easily, it is usual to bring the A phase winding axes of the torque windings in line with that of the suspension force windings. The suspension force windings are embedded in the outer layer of the stator slot, and the phase sequence arrangement is $N_{BA}\rightarrow N_{BB}\rightarrow N_{BC}$, $P_B = 2$. The torque windings are embedded in the inner layer of the stator slot, and the phase sequence arrangement is $N_{MA}\rightarrow N_{MB}\rightarrow N_{MC}$, $P_M = 1$. The motor structure diagram of the 2-4 poles BPMSM in the rotational coordinates is illustrated in Figure 4. Due to the fact that the pole pair of the permanent magnet air gap magnetic field is the same as that of the torque windings, their resultant magnetic field can similarly be considered as the products of currents in the torque windings [13]. The diagrams of the motor structure and operation principle for the 2-4 poles BPMSM, based on the conventional analysis method and on

the magnetic field equivalent current analysis method, are depicted in Figure 4a,b, respectively. The windings N_M stand for equivalent torque windings, and windings N_B represent equivalent suspension force windings. Then the principles of radial suspension force generation are compared below.

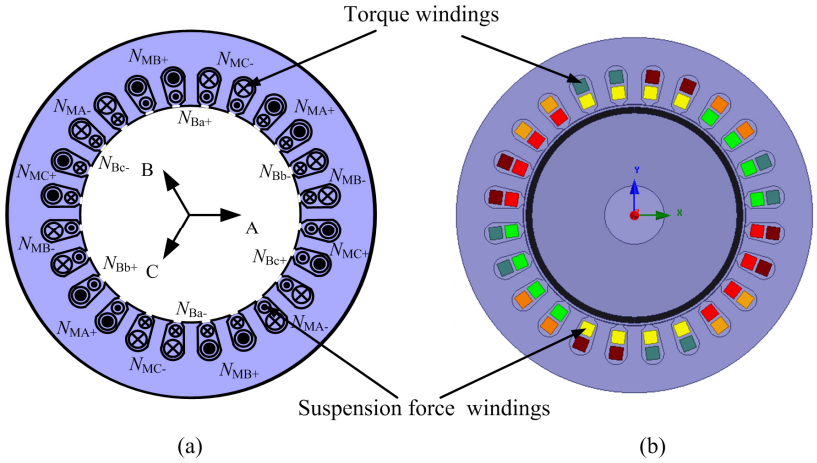

Figure 3. Structure diagram of the bearingless permanent magnetic synchronous motor (BPMSM). (**a**) Stator winding distribution. (**b**) Finite element analysis model.

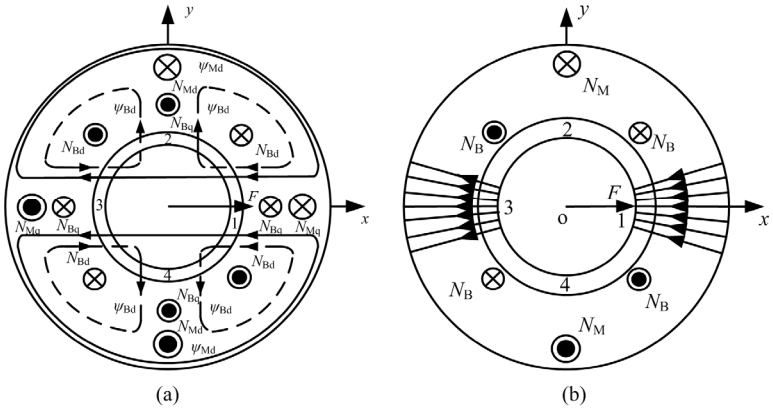

Figure 4. Structure and operation principle diagram of the 2-4 poles BPMSM. (**a**) Based on conventional analysis method. (**b**) Based on the magnetic field equivalent current analysis method.

Figure 4a illustrates the principle based on the conventional method for the BPMSM [14,15]. The symmetrical 2-pole excitation flux ψ_{Md} is generated by the *d*-axis component N_{Md} of the torque windings. When a suspension force winding current I_{Bd} is provided, the symmetrical 4-pole flux ψ_{Bd} is generated in the air gap. The directions of the torque winding fluxes ψ_{Md} and the torque winding fluxes ψ_{Bd} are same in the air gap 1, and thus, the resultant air gap flux density is increased. In the air gap 3, their flux directions are opposite, so the resultant air gap flux density is decreased. Then, according to Maxwell's stress tensor, the radial suspension force F is produced and points to the positive x-axis. The opposite-direction radial suspension force in the x-axis can be produced with a negative current I_{Bd}. Moreover, the vertical radial suspension force F in the y-axis can be produced by providing the suspension current I_{Bq} in the suspension winding N_{Bq}. In short, the directions of the radial suspension forces are affected by the phase of the 4-pole suspension force winding current.

Figure 4b depicts the principle based on the proposed magnetic field equivalent current analysis method. In the air gap 1, an intensifying factor is formed and a softening factor is formed at the position of air gap 3. The direction of the composite MMF is the positive *x*-axis. Thus, a radial suspension force *F* is generated which is oriented in the positive *x*-axis. The analysis result of the proposed method agrees with that of conventional method. In the same way, if the equivalent suspension force windings N_B rotate a 90° electrical angle in the counter-clockwise direction, the vertical radial suspension force *F* in the positive *y*-axis is generated. The radial suspension force *F* in the negative *x*-axis can be produced through rotating N_B by 180° electrical angle in the counter-clockwise direction. In conclusion, the direction of radial suspension force rotation has relations with that of equivalent suspension force winding rotation, and the rotating angular velocity is P_B times to that of equivalent suspension force windings, as can be seen in [16]. The description of the principle for the 2-4 poles BPMSM also applies to other pole pair compositions and various types of bearingless motors.

3. Analysis on Producing Stable Radial Suspension Force for the BPMSM

Based on the magnetic field equivalent current analysis method, the necessary condition to produce a stable radial suspension force in a certain direction can be derived. In this section, the counter-clockwise rotation direction is defined as the rotation positive direction. It is supposed that torque winding air gap magnetic field rotates in the positive direction with mechanical angular velocity ω_M. Then, to obtain a stable radial suspension force in a certain direction, the absolute angular velocity of the radial suspension force should be set as 0 rad/s, and its direction should be fixed. Treating the torque winding air gap magnetic field as a reference, the relative angular velocity ω_F of radial suspension force is $-\omega_M$. The relative angular velocity ω of suspension force winding air gap magnetic field can be obtained as [17]:

$$\begin{cases} \omega = -\omega_F / P_B = -(-\omega_M)/P_B = \omega_M / P_B, & P_B = P_M - 1 \\ \omega = \quad \omega_F / P_B = (-\omega_M)/P_B = -\omega_M / P_B, & P_B = P_M + 1 \end{cases} \tag{1}$$

The absolute angular velocity ω_B of suspension force winding air gap magnetic field can be written as:

$$\begin{cases} \omega_B = \omega_M + \omega = \quad \omega_M + \omega_M / P_B \quad = P_M \omega_M / P_B, & P_B = P_M - 1 \\ \omega_B = \omega_M + \omega = \omega_M + \left(-\omega_M / P_B\right) = P_M \omega_M / P_B, & P_B = P_M + 1 \end{cases} \tag{2}$$

Likewise, when the angular velocity of the torque winding air gap magnetic field is $-\omega_M$, (that is, rotating in the negative direction), the absolute angular velocity of suspension force winding air gap magnetic field can be expressed as $-P_M\omega_M/P_B$.

Therefore, the necessary condition to generate a stable radial suspension force is that the angular velocity ω_B of suspension force winding air gap magnetic field should be P_M/P_B times that of the torque winding air gap magnetic field, and their directions should remain the same. In other words, the suspension force winding air gap magnetic field and the torque air gap winding magnetic field have the same rotation electric angular velocity and rotation direction:

$$P_B \cdot \omega_B = P_B \cdot \left(P_M \omega_M / P_B\right) = P_M \cdot \omega_M \tag{3}$$

The verification of the necessary condition by means of the magnetic field equivalent current analysis method is as follows: the relative motion analysis situations are shown in Figures 5 and 6.

Among them, large dimension and small dimension of windings represent equivalent suspension force windings and equivalent torque windings, respectively.

If $P_B = P_M + 1$ (that is $P_B = 2$, $P_M = 1$), when the equivalent torque windings rotate π/2 rad mechanical angle in positive direction, according to the necessary condition, the equivalent suspension force windings must rotate $\theta_B = P_M\theta_M/P_B = \pi/4$ rad mechanical angle in the same direction, as can be seen from Figure 5b. There is an intensifying factor at $\alpha = 0$ rad and a softening factor at $\alpha = \pi$ rad. Thereby, radial suspension force is produced towards the direction of 0 rad. In this situation, the rotation electrical angle of the equivalent suspension force windings $P_B \cdot \theta_B = 2 \cdot \pi/4 = \pi/2$ rad is the same as that of the equivalent torque windings $P_M \cdot \theta_M = 1 \cdot \pi/2 = \pi/2$ rad. When the equivalent torque windings rotate π rad mechanical angle in positive direction, the equivalent suspension force windings must rotate $\theta_B = P_M\theta_M / P_B = \pi/2$ rad mechanical angle in positive direction, as shown in Figure 5c. There also is an intensifying factor at $\alpha = 0$ rad and a softening factor at $\alpha = \pi$ rad, so the direction of the radial suspension force remains 0 rad. The rotation electrical angle of the equivalent suspension force windings $P_B \cdot \theta_B = 2 \cdot \pi/2 = \pi$ rad is equal to that of the equivalent torque windings $P_M \cdot \theta_M = 1 \cdot \pi = \pi$ rad. In Figure 5d, when the equivalent torque windings rotate 3π/2 rad mechanical angle in the positive direction, the same conclusion could be obtained. In consequence, when $P_B = P_M + 1$, to generate a stable and reliable radial suspension force, the rotation electrical angular of the equivalent suspension force windings $P_B \cdot \theta_B$ is equal to that of equivalent torque windings $P_M \cdot \theta_M$. Besides, the rotation direction of equivalent suspension force windings is the same as that of equivalent torque windings, and the converse is also true.

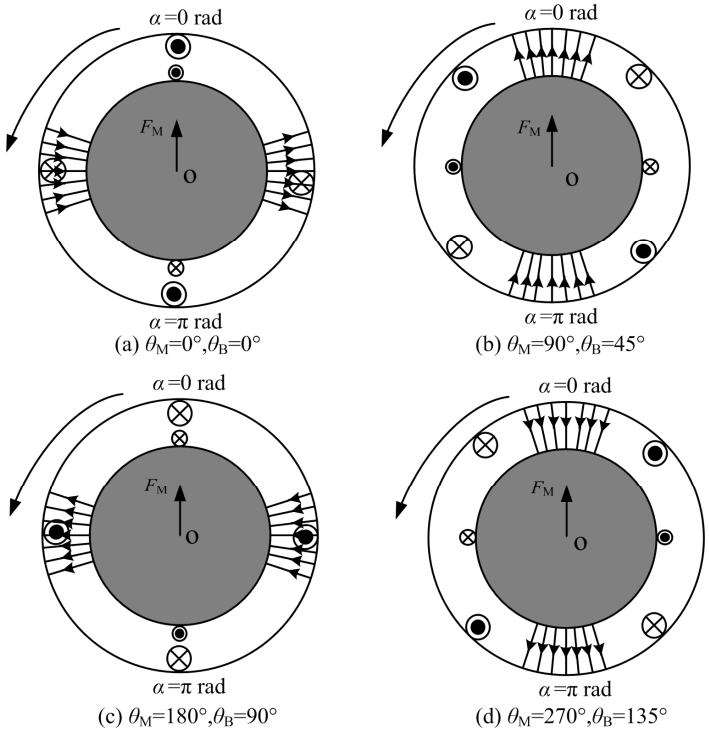

Figure 5. Schematic diagram of stable radial suspension force in a single direction ($P_B = P_M + 1$). (**a**) Initial state. (**b**) Rotation of equivalent torque windings with the mechanical angular 90°. (**c**) Rotation in the positive direction with the mechanical angular 180°. (**d**) Rotation in the positive direction at the mechanical angular 270°.

If $P_B = P_M - 1$ (that is $P_B = 1$, $P_M = 2$), when the equivalent torque windings rotate π/4 rad mechanical angle in the positive direction, the equivalent suspension force windings must rotate $\theta_B = P_M\theta_M / P_B = \pi/2$ rad mechanical angle in the same direction to hold the radial suspension force in a stationary direction, as plotted in Figure 6b. The intensifying factor is at $\alpha = 0$ rad and a softening factor is at $\alpha = \pi$ rad. Thereby, the radial suspension force points to the direction of 0 rad. Then, the rotation electrical angle of the equivalent suspension force windings $P_B \cdot \theta_B = 1 \cdot \pi/2 = \pi/2$ rad is equal to that of the equivalent torque windings $P_M \cdot \theta_M = 2 \cdot \pi/2 = \pi$ rad. When the equivalent torque windings rotate π/2 rad mechanical angle in positive direction, the equivalent suspension force windings must rotate π rad mechanical angle in positive direction, as shown in Figure 6c. The rotation electrical angle of the equivalent suspension force windings $P_B \cdot \theta_B = 1 \cdot \pi = \pi$ rad is also equal to that of equivalent torque windings $P_M \cdot \theta_M = 2 \cdot \pi/2 = \pi$ rad. In Figure 6(d), when the equivalent torque windings rotate 3π/4 rad mechanical angle in positive direction, the same conclusion could be obtained. Thus, when $P_B = P_M - 1$, the conclusion is consistent with that of the condition of $P_B = P_M + 1$.

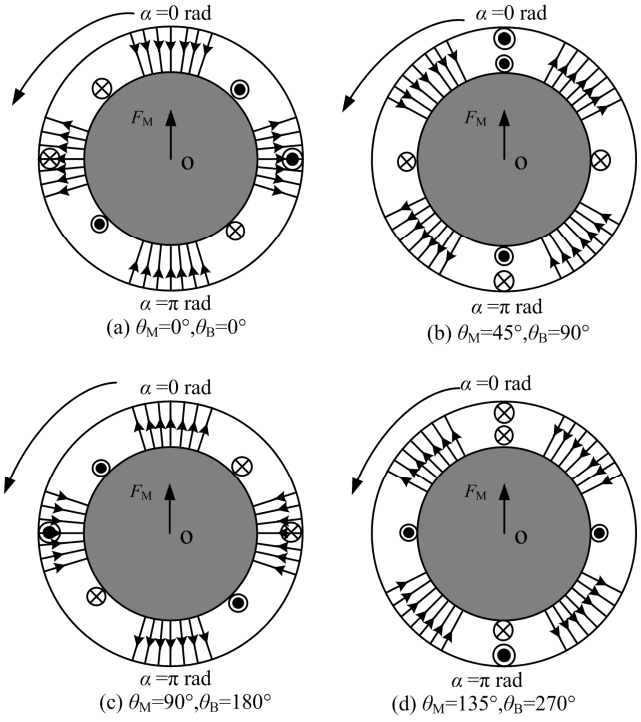

Figure 6. Schematic diagram of a stable radial suspension force in a single direction ($P_B = P_M - 1$). (**a**) Initial state. (**b**) Rotation of equivalent torque windings with the mechanical angular rotation of 45°. (**c**) Rotation in the positive direction with the mechanical angular rotation of 90°. (**d**) Rotation in the positive direction at the mechanical angular rotation of 135°.

In brief, the electrical angular velocity of torque winding air gap magnetic field $P_M \cdot \omega_M$ is in complete agreement with that of suspension force winding air gap magnetic field $P_B \cdot \omega_B$. The current frequency of suspension force windings and torque windings can be expressed as:

$$f_B = f_M = P_M \cdot \omega_M / 2\pi \quad (4)$$

Therefore, the necessary condition to generate a stable and reliable radial suspension force is that the suspension force winding air gap magnetic field rotates in the same direction as the torque winding air gap magnetic field with P_M/P_B times to the angular velocity ω_M of the torque winding air gap magnetic field.

4. Mathematical Model of Radial Suspension Force for the BPMSM

4.1. Analytical Model of Radial Suspension Force for the BPMSM

According to Maxwell's stress tensor method, the radial suspension force vector F as shown in Figure 5b can be expressed as [3,18]:

$$F = \begin{pmatrix} F_n \\ F_t \end{pmatrix} = \frac{1}{2\mu_0} \oint_A \begin{pmatrix} B_n^2 - B_t^2 \\ 2B_n B_t \end{pmatrix} \mathrm{d}A = \frac{lr}{2\mu_0} \int_0^{2\pi} \begin{pmatrix} B_n^2 - B_t^2 \\ 2B_n B_t \end{pmatrix} \mathrm{d}\theta \tag{5}$$

with μ_0 as the air permeability, B_n and B_t being the radial and tangential components of air gap flux density for the BPMSM, respectively, A being the stator inner surface area, r as the stator inner diameter, l representing the motor length and θ being the space angle.

Taking only the fundamental components of current into account, the air gap flux density B_1 caused by a permanent magnet and torque winding current loading A_1, and the air gap flux density B_2 excited by a suspension force winding current loading A_2 can be described as:

$$\begin{aligned} B_1(t,\theta) &= B_{1\mathrm{m}} \cos(\omega_1 t - P_M \theta + \lambda_1) \\ B_2(t,\theta) &= B_{2\mathrm{m}} \cos(\omega_2 t - P_B \theta + \lambda_2) \end{aligned} \tag{6}$$

while the current loadings of torque windings and suspension force windings A_1, A_2 can be expressed as follows:

$$\begin{aligned} A_1(t,\theta) &= -A_{1\mathrm{m}} \sin(\omega_1 t - P_M \theta + \lambda_1) \\ A_2(t,\theta) &= -A_{2\mathrm{m}} \sin(\omega_2 t - P_B \theta + \lambda_2) \end{aligned} \tag{7}$$

where: $B_{1\mathrm{m}} = \frac{\mu_0}{\delta}\left(\frac{3}{2}\frac{4}{\pi}\frac{I_{1\mathrm{m}}}{2}\frac{N_1 g_M}{P_M}\right)$, $B_{2\mathrm{m}} = \frac{\mu_0}{\delta}\left(\frac{3}{2}\frac{4}{\pi}\frac{I_{2\mathrm{m}}}{2}\frac{N_2 g_B}{P_B}\right)$, $A_{1\mathrm{m}} = \frac{mN_1 I_{1\mathrm{m}} g_M}{\pi r}$, $A_{2\mathrm{m}} = \frac{mN_2 I_{2\mathrm{m}} g_B}{\pi r}$. $\delta_0 = h_\mathrm{m} + g$ is the equivalent air gap length without rotor eccentricity, h_m is the permanent magnet thickness, g is the mechanical air gap length, g_M and g_B correspond to the fundamental winding factors of torque windings and suspension force windings, respectively, P_M and P_B are their pair poles. $I_{1\mathrm{m}} = I_M + I_f$ is the torque winding resultant current magnitude, I_M and I_f represent as the magnitude of the torque winding current and the equivalent current of the permanent magnets, respectively. $I_{2\mathrm{m}}$ is the suspension force winding current value. N_1, N_2 are the turn numbers of torque windings and suspension force windings, respectively, ω_1 and ω_2 correspond to their electrical angular frequencies, λ_1 and λ_2 are their initial phase angle.

The radial flux density component B_n and tangential flux density component B_t in the air gap are given by:

$$\begin{aligned} B_n(t,\theta) &= B_1(t,\theta) + B_2(t,\theta) \\ B_t(t,\theta) &= \mu_0 A(t,\theta) \end{aligned} \tag{8}$$

Supposing $P_M = P_B \pm 1$ and $\omega_1 = \omega_2$, the radial suspension force components in the x- and y-direction are obtained as:

$$\begin{aligned} F_x &= \pi \cdot l \cdot r\left(\frac{B_{1m}B_{2m}}{2\mu_0} \pm \left(\frac{B_{1m}A_2}{2} - \frac{B_{2m}A_1}{2}\right)\right)\cos(\gamma_1 - \gamma_2) = (k_m \pm k_l) I_{1m} I_{2m} \cos(\gamma_1 - \gamma_2) \\ F_y &= \pi \cdot l \cdot r\left(\pm\frac{B_{1m}B_{2m}}{2\mu_0} + \left(\frac{B_{1m}A_2}{2} - \frac{B_{2m}A_1}{2}\right)\right)\sin(\gamma_1 - \gamma_2) = (\pm k_m + k_l) I_{1m} I_{2m} \sin(\gamma_1 - \gamma_2) \end{aligned} \quad (9)$$

where $k_m = \frac{9}{2\pi}\frac{\mu_0 l r N_1 N_2 g_M g_B}{P_M P_B \delta_0^2}$, $k_l = \frac{3}{2\pi}\frac{m\mu_0 l N_1 N_2 g_M g_B}{P_M P_B \delta_0}$ and m is the phase number for the BPMSM.

The first part is the Maxwell controllable suspension forces influenced by the air gap flux density B_1 and B_2, whereas the second part is the radial component of the Lorentz forces generated by the interaction of the air gap flux density B_1 with the current loading A_2 and the interaction of the air gap flux density B_2 with the current loading A_1. It can be seen from (9) that the amplitude of the controllable radial suspension forces is linear with the suspension force winding current value I_{2m}. And the direction depends only on phase difference between the torque winding air gap flux density B_1 and suspension force winding air gap flux density B_2, given by λ_1–λ_2. Due to $r >> \delta_0$ for the BPMSM, k_l is much less than k_m, thus the radial component of Lorentz forces can be ignored.

Therefore, under dq synchronous rotating reference frame, the radial suspension force F_d and F_q can be expressed as:

$$\begin{pmatrix} F_d \\ F_q \end{pmatrix} = k_m \begin{pmatrix} I_{Md} + I_f & I_{Mq} \\ I_{Mq} & -(I_{Md} + I_f) \end{pmatrix} \begin{pmatrix} I_{Bd} \\ \pm I_{Bq} \end{pmatrix} \quad (10)$$

with the I_{Md} and I_{Bd} as the d-axis components of torque and suspension force winding currents, the I_{Mq} and I_{Bq} corresponding to their q-axis components, respectively.

Except for currents in the suspension force windings, the rotor eccentricity e will also cause a radial suspension force, namely, unilateral magnetic force. When rotor eccentric displacement occurs, the motor air gap length δ will change which can be approximately expressed as:

$$\delta(\theta, t) \approx \delta_0 - e\cos(\theta - \varphi) = \delta_0 - x\cos\theta - y\sin\theta \quad (11)$$

with $x = e\cos\varphi$, $y = e\sin\varphi$, and φ being the deviation angle between the eccentricity orientation and x-axis. Thus, the radial suspension force can be expressed by [19,20]:

$$\begin{pmatrix} F_x \\ F_y \end{pmatrix} = \begin{pmatrix} F_d \\ F_q \end{pmatrix} + \begin{pmatrix} F_{ed} \\ F_{eq} \end{pmatrix} = k_m \begin{pmatrix} I_{Md} + I_f & I_{Mq} \\ I_{Mq} & -(I_{Md} + I_f) \end{pmatrix} \begin{pmatrix} I_{Bd} \\ \pm I_{Bq} \end{pmatrix} + k_{ecc} \begin{pmatrix} x \\ y \end{pmatrix} \quad (12)$$

Here, $k_{ecc} = \frac{9}{2}\frac{\mu_0 l r N_1^2 g_M^2 I_1^2}{\pi P_M^2 \delta_0^3}$.

In order to support the stable suspension, it is necessary to compensate the unilateral magnetic forces by a reasonable adjustment of the suspension force winding currents.

4.2. Analytical Model of Electromagnetic Torque for the BPMSM

Because the d- and q-axis components of the torque winding inductances are approximately equal ($L_d = L_q$) for the surface-mount BPMSM, the mathematical formula of electromagnetic torque has the

same form as the conventional PMSM in a *dq* synchronous rotating reference frame which can be given by [21]:

$$T_{em} = P_{\mathrm{M}}\psi_{1d}I_{1q} + P_{\mathrm{M}}(L_d - L_q)I_{1d}I_{1q} = P_{\mathrm{M}}\psi_{1d}I_{1q} \tag{13}$$

where, $\psi_{1d} = \psi_{\mathrm{M}d} + \psi_{fd}$, $\psi_{1q} = \psi_{\mathrm{M}q} + \psi_{fq}$, ψ_{1d} and ψ_{1q} are the *d*- and *q*-axis components of the equivalent torque winding air gap flux linkage, respectively. ψ_{Md} and ψ_{Mq} are *d*- and *q*-axis components of the torque winding air gap flux linkage, respectively. ψ_{fd} and ψ_{fq} are *d*- and *q*-axis components of the air gap flux linkage excited by the permanent magnet.

4.3. FEA Validation of the Model

To verify radial suspension force generation, the 2D FEA simulation model is developed by means of the software-ANSYS (ANSYS Inc., Cecil Township, PA, USA) for the BPMSM, as shown in Figure 3b. The main specifications of the BPMSM simulation model are listed in Table 1.

Table 1. Specification of the prototype machine.

Parameter	Symbol	Vaule
Motor unit geometry and torque system data		
Rated mechanical power	P_{N}	500 W
Stator slot count	Q	24
Stator inner diameter	d_{si}	75 mm
Stator outer diameter	d_{so}	120 mm
Rotor outer diameter	d_{ro}	73 mm
Auxiliary bearing thickness	h_{a}	0.7 mm
Pole pair count	P_{M}	1
Torque winding wire diameter	Φ	0.71 mm
Turns of torque winding per one slot	N_{M}	22
Stacking coefficient	k_{s}	0.95
Number of winding parallel ways	a_{M}	1
Winding connection	Y	-
Mechanical air gap length	g	1 mm
Permanent magnetic material	-	NdFeB
Coercive force	H_{c}	−890 kA/m
Magnet thickness	h_{m}	2 mm
Magnet remanence at 20°C	B_{r}	1.1 T
Suspension force system data		
Pole pair count	P_{B}	2
Turns of suspension force winding per one slot	N_{B}	22
Number of winding parallel ways	a_{B}	1
Winding connection	Y	-
Force/current coefficient	k_m	122.325 N/A
Force/displacement coefficient	k_{ecc}	568.02 N/mm

In Figures 7–9, the FEA results of the radial suspension force are compared with the mathematical model calculation values. This leads to the following conclusions: the amplitudes of the radial

suspension force increase with the suspension force winding current I_{2m}, as illustrated in Figure 7a. When the suspension force winding current I_2 is small (less than 3 A), the radial suspension forces show a linearly increasing trend. The FEA results are in good agreement with the mathematical model calculations and the error between them is less than 3 percent, as depicted in Table 2. When the current has reached 3 A, the motor core enters a saturated state. Thus the FEA results are significantly less than the values of the mathematical model calculation, and the error between them is more than 10 percent, so the rated suspension force current is set at 2 A in this paper, and the maximum radial suspension force available in this case is 244.65 N. Besides, from Figure 7b, it can be seen that the direction of the radial suspension force is proportional to the initial phase angle λ_2 of the suspension force winding current. It is almost unaffected by saturation of the magnetic circuit which is completely consistent with the mathematical model calculation values. In conclusion, when the motor operates in a linear state, the amplitude and direction of the radial suspension force change with the magnitude and phase angle of the suspension force winding current, respectively. On the basis of this rule, the orientation control of radial suspension force can be realized, which can build a foundation for the BPMSM.

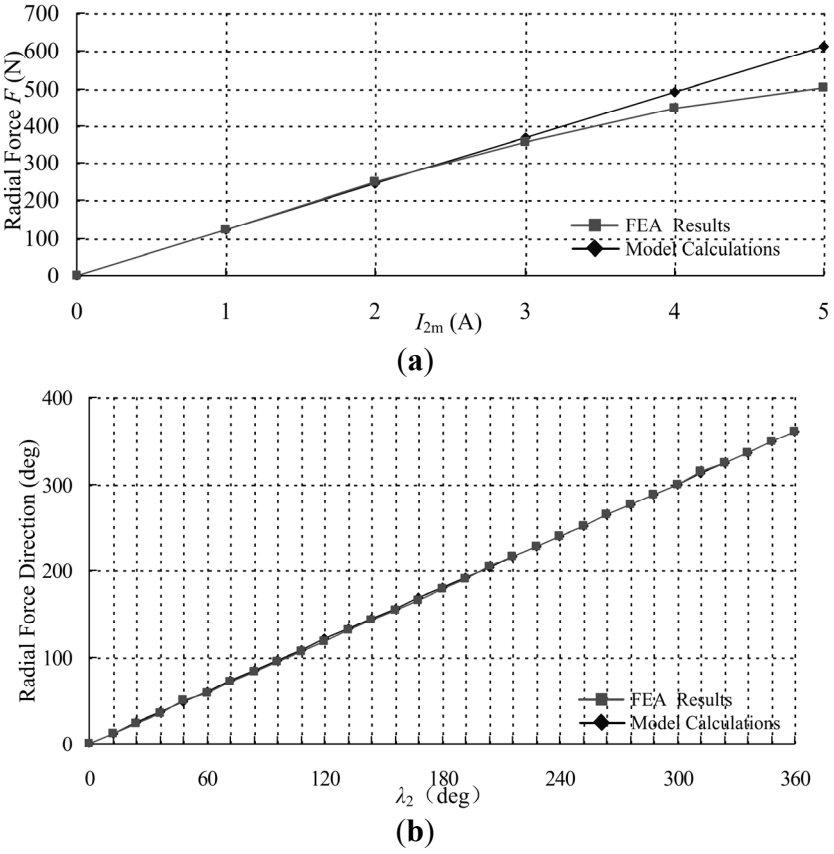

Figure 7. Relationships between radial suspension forces and suspension currents. (**a**) Radial suspension force *versus* I_{2m} (I_{1m} = 0 A, λ_2 = 0 deg), (**b**) Radial suspension force *versus* λ_2 (I_{1m} = 0 A, I_{2m} = 2 A). FEA—Finite Element Analysis.

In Figure 8, the radial suspension force component in the *x*-direction changes in cosines with initial phase angle λ_2 of suspension force winding current, and the *y*-direction component is dominated by the sines rule with initial phase angle λ_2. The variation tendencies of the FEA results and mathematical

model calculations are essentially identical. When the suspension force winding current is zero, the related FEA for a unilateral magnetic force is carried out, as shown in Figure 9.

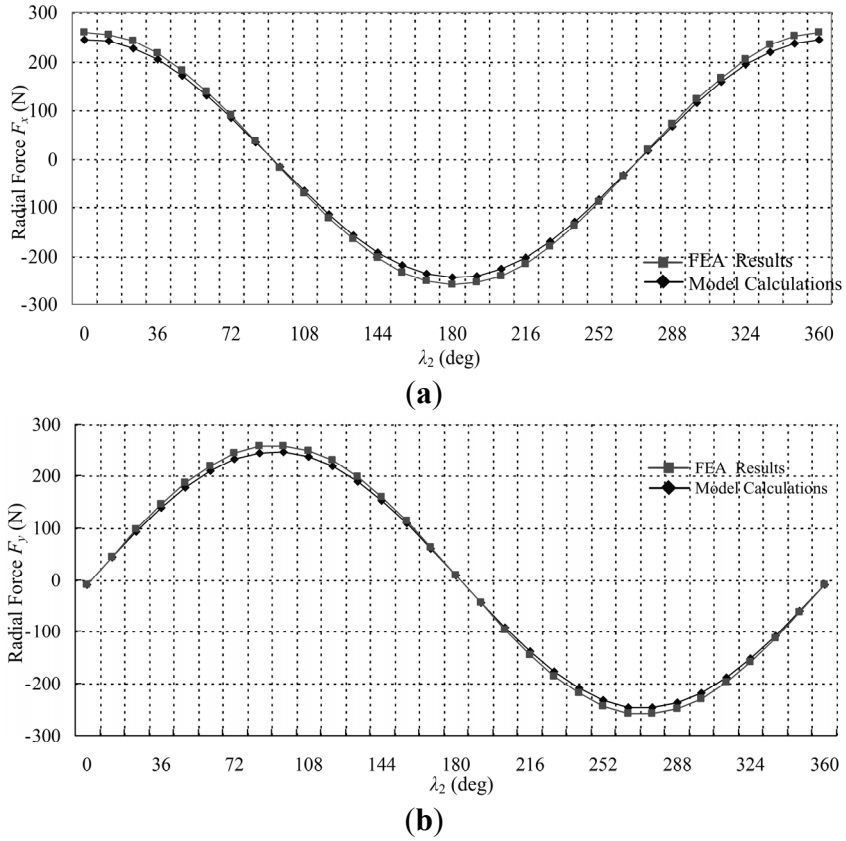

Figure 8. Effects of suspension force winding spatial position angle λ_2 on suspension force. (**a**) Radial suspension force F_x *versus* λ_2 (I_1 = 0 A, I_2 = 2 A), (**b**) Radial suspension force F_y *versus* λ_2 (I_1 = 0 A, I_2 = 2 A).

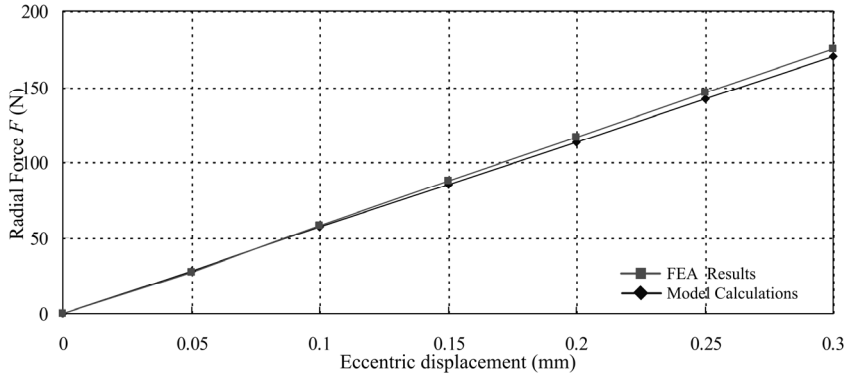

Figure 9. Relationship between unilateral magnetic force and eccentric displacement of rotor (I_1 = 0 A, I_2 = 0 A).

Table 2. Comparison of FEA and mathematical models in controllable radial suspension forces.

I_{Bm} (A)	The FEA results (N)	Mathematical model values (N)	Error
1	123.5032	122.325	0.96%
2	247.6507	244.65	1.23%
3	365.9582	366.975	2.73%
4	448.0844	489.3	8.42%
5	501.6163	611.625	17.99%

It's concluded that the FEA results basically agree well with the mathematical model calculation values, and the error between them is less than 2.7 percent (Table 3). Due to the assembly auxiliary bearing, the maximum rotor radial deviation ranges from −0.3 mm to 0.3 mm, and the amplitude of maximum unilateral magnetic force is 175 N.

Table 3. Comparison of FEA and mathematical model in unilateral magnetic force.

Eccentric displacement (mm)	The FEA results (N)	Mathematical model values (N)	Error
0.1	28.4	27.34	1.99%
0.2	113.604	116.462	2.51%
0.3	170.46	174.953	2.67%

5. Experimental System for the BPMSM

5.1. Prototype Machine Structure

The 5-DOF suspension control for the BPMSM is an essential prerequisite to realize its high-speed and stable operation. The prototype BPMSM, consisting of a 3-DOF axial-radial magnetic bearing and a 2-DOF BPMSM, has been built, as shown in Figure 10.

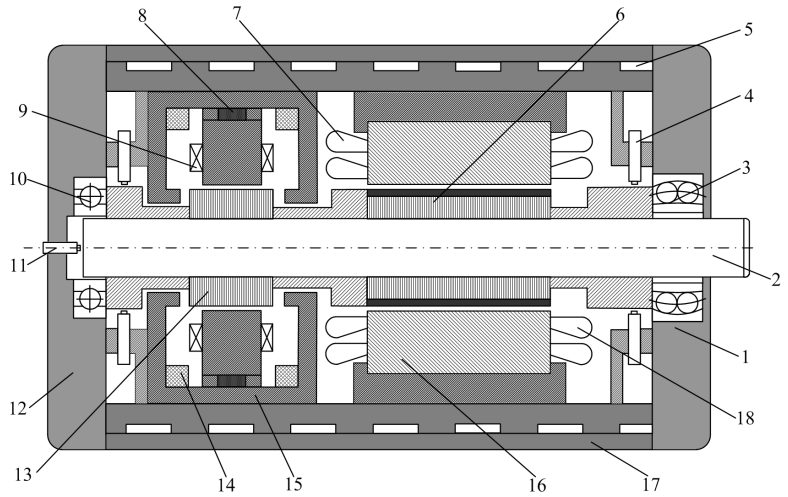

Figure 10. Schematic drawing of a test machine: 1-Front cover, 2-Shaft, 3-Radial-axial auxiliary bearing, 4-Radial displacement sensor, 5-Internal thread cooling pipe, 6-Permanent magnet rotor, 7-Suspension force winding overhang, 8-Permanent magnet, 9-Radial control windings, 10-Radial auxiliary bearing, 11-Axial displacement sensor, 12-Bake cover, 13-Rotor, 14-Axial control windings, 15-Axial stator lamination, 16-Stator lamination, 17-Aluminium housing, 18-Torque winding overhang.

The 2-DOF on the right end of the high-speed machine and the rotor rotation are controlled by the BPMSM unit, while the other 2-DOF on the left end and the axial direction are controlled by the 3-DOF axial-radial magnetic bearing unit. Among them, the BPMSM unit is the key technology to realize the stable operation of the high-speed machine. Thus, this paper mainly focuses on the 2-DOF BPMSM unit.

The stator and rotor iron core are wire cut from DW465_50 silicon steel sheet and neodymium-iron-boron (NdFeB) is selected as the permanent magnet material. The rotor radial positions are measured by eddy-current displacement sensors and the rotation speed is measured by a photoelectric encoder. If there is no external disturbance or load imposed on the rotor, the radial suspension force just supports the rotor in the balance position.

5.2. Control of Torque and Radial Suspension Force for the BPMSM

The air gap magnetic field of the BPMSM is composed of the suspension force winding air gap magnetic field, torque winding air gap magnetic field and permanent magnet air gap magnetic field. The torque production mechanism is the same as that of PMSM, namely, the product of the interactions of the permanent magnet and torque winding air gap magnetic field. In addition, because of its long effective air gap length for the surface-mounted BPMSM, the torque winding air gap magnetic field can be ignored compared with the permanent magnet air gap magnetic field. Then, the radial suspension force could be considered as the interactions between the suspension force winding air gap magnetic field and permanent magnet air gap magnetic field. Thus, the decoupling control between torque and radial suspension force can be realized by adoption of the traditional FOC [22].

Figure 11 shows the relative position between torque windings and suspension force windings. In order to facilitate the control of the radial suspension force, the *xoy* coordinate is set up along the displacement sensors. It is supposed that the angle between the *x*-axis and A phase axes of the torque windings ($P_M = 1$) or the nearest A phase axes relative to the positive *x*-axis ($P_M > 1$) is θ_M, and the angle between the *x*-axis and A phase axes of suspension force windings ($P_B = 1$) or the nearest A phase axes relative to the positive *x*-axis ($P_B > 1$) is θ_B. If $\theta_M \neq \theta_B$, defining $\Delta\theta = \theta_B - \theta_M$, (see Figure 11a). An advanced mechanical angle $\Delta\theta$ must be compensated by the suspension force winding currents. Based on the relative position relations between the suspension force winding air gap magnetic field and the torque winding air gap magnetic field, the result is equivalent to $\Delta\theta = 0°$, (see Figure 11b). If $P_B = P_M + 1$, the advanced electrical angle θ_l must be compensated by the suspension force winding currents. If $P_B = P_M - 1$, the lag electrical angle θ_l must be compensated by the suspension force winding currents. Thus, the suspension force winding air gap magnetic field and torque winding air gap magnetic field have the same direction of rotation and electric angular velocity. In the control system, the suspension force winding current command i_{Bd} will directly control the component of the radial suspension force in the *x*-axis. Then, due to the current component i_{Bq} advancing i_{Bd} with mechanical angle $90°/P_B$, if $P_B = P_M - 1$, the current component i_{Bq} will generate a radial suspension force lagging 90° with respect to the *x*-axis. If $P_B = P_M + 1$, the current component i_{Bq} will produce a radial suspension force advancing 90° with respect to the *x*-axis. Consequently, the 2-DOF radial suspension force control for the BPMSM can be realized.

When the BPMSM runs at load states, the torque winding current component i_{Mq} will produce an air gap magnetic field in the q-axis. Then, an advancing electrical angle of θ_1 (< 90°) is produced by the torque winding air gap magnetic field. In other words, the suspension force winding air gap magnetic field lags a mechanical angle θ_1/P_M with respect to the torque winding air gap magnetic field. If $P_B = P_M + 1$, the angle of suspension force is $\theta_1/P_M + (-P_B\theta_1/P_M) = -\theta_1$. To obtain a stable suspension force, an advancing mechanical angle θ_1/P_B must be compensated by the suspension force winding currents. If $P_B = P_M - 1$, the angle of radial suspension force is $\theta_1/P_M + P_B\theta_1/P_M = \theta_1$. Similarly, an advancing mechanical angle θ_1/P_B must be compensated by the suspension force winding currents. The advanced angle θ_1 of the torque winding current can be obtained by the proportional relation the air gap magnetic field of torque winding current component i_q and the original torque winding air gap magnetic field.

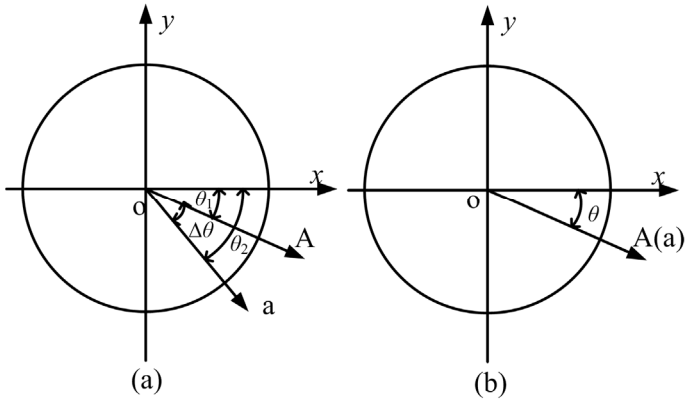

Figure 11. Relative positions of torque windings and suspension force windings.

Based on the rotor flux-orientation control, it is concluded that:

$$\begin{aligned} &I_{Md} = 0, \;\; I_{1d} = I_f, \;\; I_{1q} = I_{Mq} \\ &\psi_{fd} = \psi_f, \psi_{fq} = \; 0 \end{aligned} \tag{14}$$

Thus, Equations (12) and (13) can be expressed respectively as:

$$\begin{pmatrix} F_x \\ F_y \end{pmatrix} = k_m \begin{pmatrix} I_f & I_{Mq} \\ I_{Mq} & -I_f \end{pmatrix} \begin{pmatrix} I_{Bd} \\ \pm I_{Bq} \end{pmatrix} + k_{ecc} \begin{pmatrix} x \\ y \end{pmatrix} \tag{15}$$

$$T_{em} = P_M \psi_f I_{Mq} \tag{16}$$

Hence, the radial suspension forces and torque are controlled by changing the suspension force winding current (I_{Bd}, I_{Bq}) and torque winding current (I_{Mq}), respectively. Moreover, compared with CRPWM, the space vector pulse width modulation (SVPWM) method can reduce the inverter switching frequency and decrease the harmonic content of the inverter output current. Hence, a control strategy based on the SVPWM method is proposed to realize the FOC in this section. Figure 12 shows the vector control block diagram, which consists of two basic schemes, namely, torque control and radial suspension force control.

In torque control, the rotational speed signal n is obtained by an optical-electricity encoder in the torque control system. The error between the speed command n^* and measurement n is amplified in

the proportional-integral (PI) controllers, and the torque winding current command i_{Mq}* can be generated by the torque control algorithm. Due to the adoption of field orientation control, the torque current commands i_{Md}* is defined as zero. Then, the reference voltage vectors $V_{M\alpha}$* and $V_{M\beta}$* can be generated through the current PI controllers and PARK inverse transformation. Finally, through the SVPWM modulation module, six PWM signals are generated to drive the voltage source inverter.

In radial suspension force control, the radial displacement closed-loop control is adopted as well as the current closed-loop control. The radial positions x and y of the rotor are measured by eddy current sensors. The error between the displacement commands and measurements is amplified in the proportional-integral-differential (PID) controllers. Thus, radial suspension force commands F_x* and F_y* are generated. Through the radial suspension force control algorithm, the F_x* and F_y* are transformed into the current commands i_{Bd}* and i_{Bq}* under the *d-q* rotating coordinate system. Then, the reference voltage vectors $V_{B\alpha}$* and $V_{B\beta}$* can be obtained through the current PI controllers and PARK inverse transformation. Finally, through the SVPWM modulation module, 6 PWM signals are produced to drive the voltage source inverter.

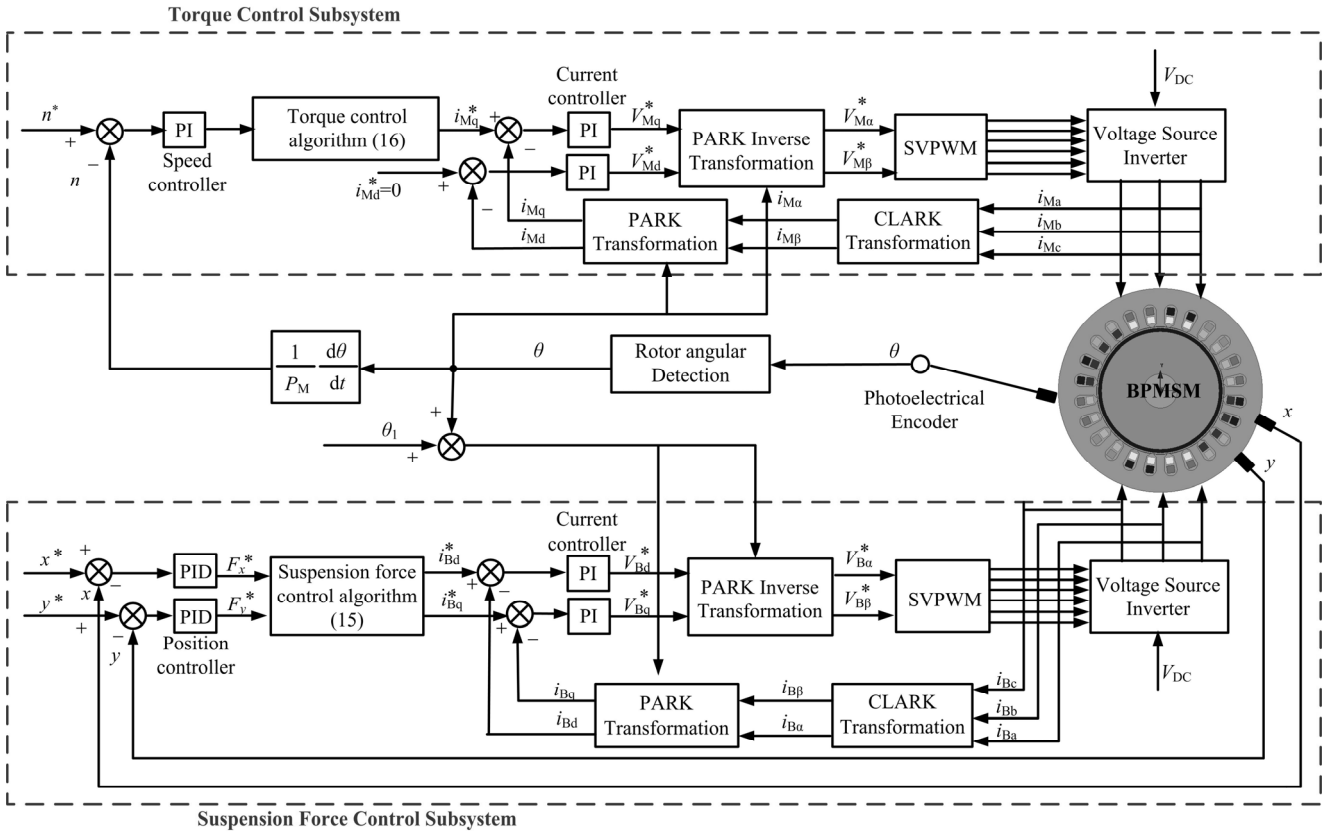

Figure 12. A vector control block diagram of BPMSM.

On the basis of the above analyses, the double closed control circuits are used both in the torque control and radial suspension force control systems. Thereinto, PID controller tuning is one of the key and more difficult points for stable suspension operation. In this paper, the engineering tuning method is adopted, due to its advantages of simplicity, valid and easy operation. Below, the specific setting steps are given. Firstly, set the integral gain k_i and differential gain k_d to zero, increase the proportional gain k_p until the output of the loop starts to oscillate. Then the k_p should be set as 0.6–0.7 times the

current value. Increase the integral gain k_i until the loop oscillates as well, and the k_i should be set as 1.5–1.8 times the current value. Then, keep k_i unchanged and change the value of k_p for tracking control. If the condition is improved, continue to adjust the k_p until a satisfactory result is achieved. Otherwise increase the original k_p a bit, adjust the k_i to improve the control effect. Repetition goes on until the best coefficients of the integral gain k_i and the proportional gain k_p are achieved. Follow the same steps above, the appropriate differential gain k_d can also be obtained.

6. Analysis on Experimental

To verify the validity of the proposed analysis method, relevant experiments are designed and conducted for the surface-mounted BPMSM. The basic parameters of the experimental prototype are as follows: rated power P_N is 500 W, rotor outer diameter d_{ro} is 73 mm, permanent magnet thickness h_m is 2 mm, air gap length g is 1 mm, torque winding resistance is 2.07 Ω, the d- and q-axis inductance of the torque windings are 8 mH, suspension force winding resistance is 1.13 Ω, the d- and q-axis inductance of the suspension force windings are 3.6 mH, the mutual inductance between torque and suspension force windings is 0.16 mH, air gap length g_1 with the auxiliary bearing is 0.3 mm.

Figure 13 shows an experiment system which takes a TMS320F2812 digital signal processor as the BPMSM drive controller, and an intelligent power module (IPM) as its power driver [23,24]. Besides, the range of analog input voltage is 0–3V in the digital converter of DSP board, but the output voltage of the displacement sensor QH8500 ranges from −2 V to −18 V and the output range of the CNSE151-100 Hall sensor is −24 mA–24 mA. Thus, the corresponding signals detected by the sensors must be transferred to the DSP board through the corresponding interface circuit. After that, when the rotor is located in the equilibrium position, the output voltage is set as 1.5 V. The output voltage should be 3 V when the rotor is located at the maximum displacement with the positive x-axis and y-axis, while the output voltage should be 0 V when the rotor is located at the minimum displacement of the negative x-axis and y-axis.

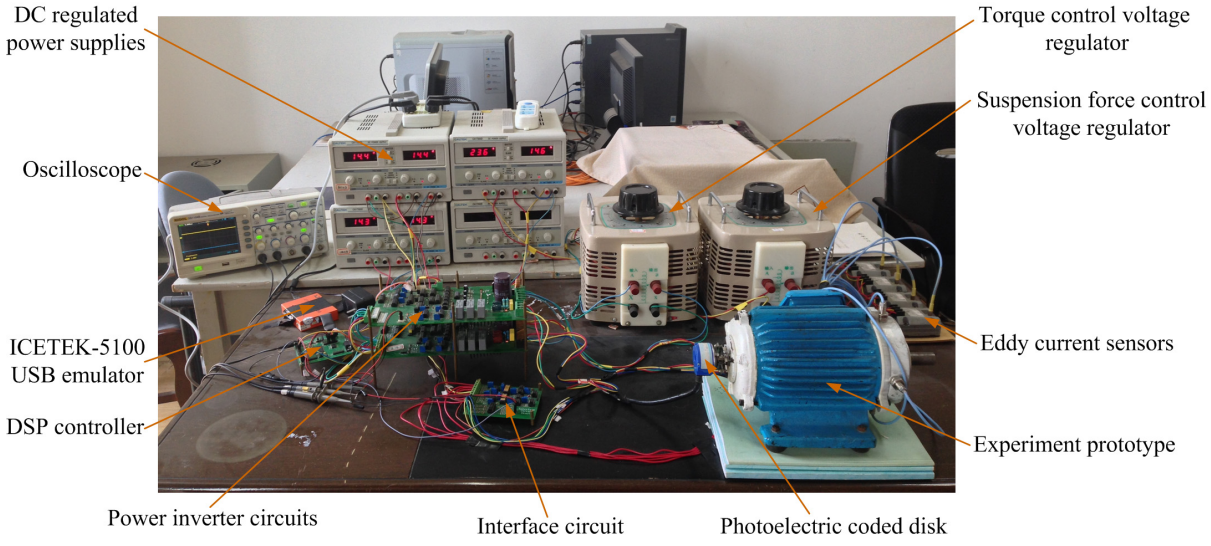

Figure 13. Experimental system of the prototype motor. DC — direct current; DSP—Digital Signal Processor.

The voltage signal is linear with the rotor displacement in the other position. Based on this method, the radial position of rotor can be detected accurately. Besides, the current interface circuit must be employed to transform the sensor output signal to the range of 0–3 V. Finally, the PID controller parameters can be achieved by the method above: in the torque control system, the current closed loop k_p is 0.6, and k_i is 0.04, the speed closed loop k_p is 0.6, and k_i is 0.00005; in the suspension force control system, the current closed loop k_p is 0.90, and k_i is 0.005, the displacement closed loop k_p is 1.8, k_i is 0.006 2, and k_d is 0.85.Then, the suspension operation tests are carried out to verify the effectiveness of the proposed equivalent winding current analysis method. Figure 14 shows the radial displacement waveforms in the *x*- and *y*-direction with the start of suspension.

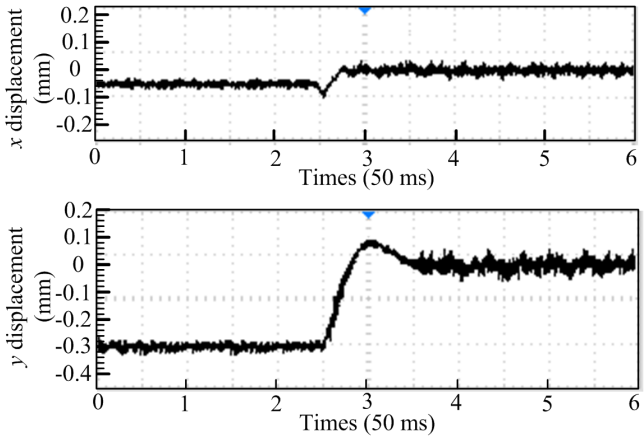

Figure 14. Radial displacement waveforms in the *x*- and *y*-direction when the start of levitation.

When the radial suspension force control system is not active, the rotor stops on a random position of the auxiliary bearing due to the influence of gravity. From Figure 14, it can be found that the original position of the rotor is (−0.05 mm, −0.3 mm). When the radial suspension force control system is active, the rotor comes rapidly back to the equilibrium position (0 mm, 0 mm). At this time, the rise time in the *y*-direction is 0.3 s, the settling time is 1 s, and the maximum deviation is 67 μm, thus the maximum overshoot is less than 22.67%, which is much smaller than the air gap at the equilibrium point (g_0 = 0.3 mm). In the *x*-direction, the vibration amplitude is about 20 μm, and the vibration amplitude is almost 32 μm in the *y*-direction. The deviations of radial displacements, which are mainly caused by mass unbalance of the rotor, are acceptable. The deviations can be reduced by more precise control schemes with an unbalance compensation circuit. The frequency of the radial displacement vibration is dependent on the rotating speed of the rotor. Figures 15–17 show the rotor position angle and rotation speed waveforms, the radial displacement waveforms in the *x*- and *y*-direction, and the waveform of relationship between them, respectively, when the rated currents are applied. In Figure 15, the rotor position angle changes periodically with time in the range of 0°–360°. The corresponding frequency is 50 Hz, which is in agreement with the rotational speed calculation formula, and the oscillation of the rotational speed is slight. Thereby, the reasonable operating characteristic of speed closed loop is verified at the speed of 3000 r/min.

From Figure 16 and Figure 17 the maximal displacement in the positive *x*-axis is about 16 μm and 12 μm in the negative *x*-axis. The maximal displacement in the positive *y*-axis is about 18 μm and 21 μm in the negative *y*-axis, when the rotor runs steadily at 3000 r/min. They are significantly

less than the length of air gap at the equilibrium point. It is found that the steady suspension characteristics of proposed 2-4 BPMSM can be obtained at 3000 r/min. Due to the effects of gravity, the displacements in the *y*-direction are larger than that in the *x*-direction. Thus, the eccentric displacement track diagrams are nearly-circular or elliptical, as shown in Figure 17.

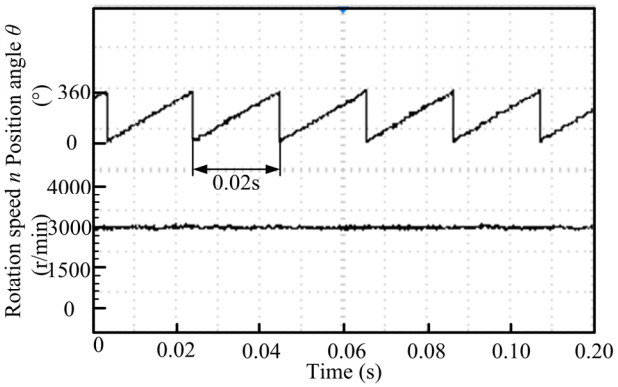

Figure 15. Waveform of the rotor position angle and rotation speed when the stable suspension operation is realized.

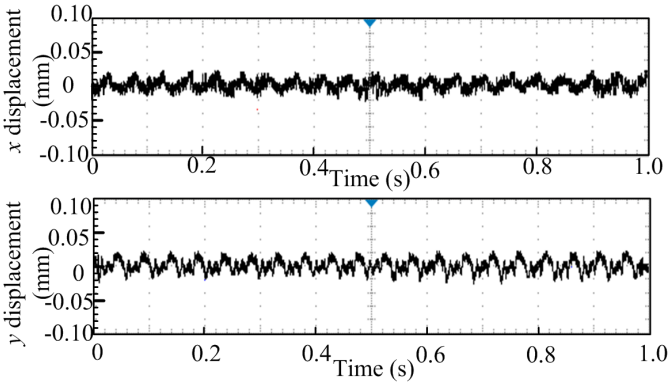

Figure 16. Radial displacement waveforms in the *x*- and *y*-direction when the start of levitation.

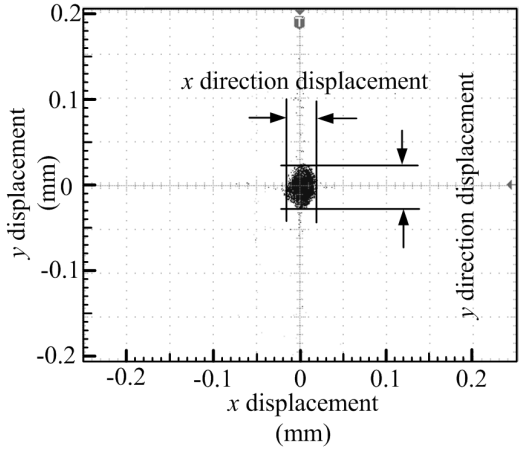

Figure 17. The relationships between radical displacements in the *x*- and *y*-direction for BPMSM.

Figure 18 describes the responses of radical displacement in the *x*- and *y*-direction when the rotation speed is changed from 1200 r/min to 3000 r/min. It can be found that the rotational speed command *n**

is accelerated suddenly from 1200 r/min to 3000 r/min at 0.4 s. After a 0.2 s settling time, the stable suspension operation is realized and the overshoot is 0. The short working time of the proposed experimental prototype shows that the dynamic response of the BPMSM is good. At this point, there is a little vibration in the *x*- and *y*-direction when the speed has been changed. But the changes of vibration amplitudes for the radical displacements which may originate from the motor's unbalance mass are slight. The vibration peak-to-peak value is about 28 μm in the *x*-direction, and the peak-to-peak value is almost 39 μm in the *y*-direction. The radial displacement deviations are within acceptable ranges, which can be reduced further by more precise control schemes with an unbalance compensation circuit, so the independent control between radial displacement and rotating speed can be realized. The validity and feasibility of the control strategy is confirmed, which establishes a solid foundation for further deliberation and research, and has some theoretical and practical reference value.

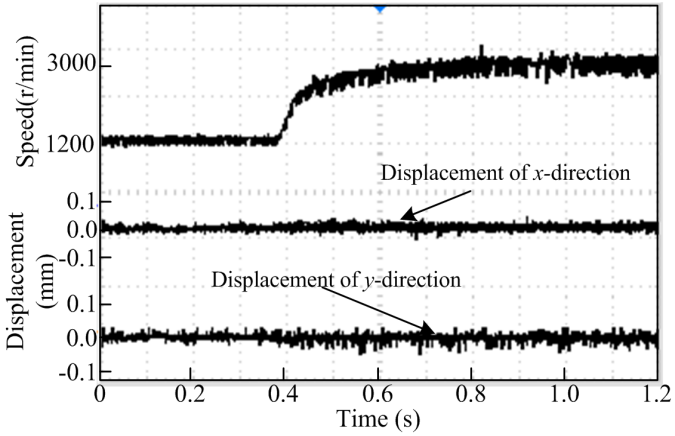

Figure 18. The responses of speed and radical displacement in the *x*- and *y*-direction when the rotation speed is changed.

7. Conclusions

This paper proposes an analysis method based on equivalent winding currents. On that basis, the validity of the necessary conditions to produce a stable radial suspension force for bearingless motors is proved. The simulation model is established by the ANSYS simulation software and the simulation results verify the theoretical analysis. In addition, good rotation and suspension performance are obviously shown by the simulation and experimental results, as well as the accuracy of the proposed analysis method and the feasibility of the control strategy. Besides, the decoupling control between electromagnetic torque and radial suspension force is also successfully achieved. Thus, the new analysis method of the BPMSM has some theoretical significance and practical reference value for further research compared with other methods.

Acknowledgments

This work was sponsored by National Natural Science Foundation of China (60974053, 61174055), Jiangsu Province University Achievements in Scientific Research Industrial Production Advancement Project (JHB2012-39), Jiangsu Province "Qinglan Project" (2014), and Jiangsu Province "333 Project" (2014).

Author Contributions

Huangqiu Zhu proposed the analysis method, performed simulation analysis, and drafted the manuscript. Hui Li designed the control strategy and helped refinement the manuscript. All authors discussed the results and approved the final manuscript.

Conflicts of Interest

The authors declare no conflict of interest.

References

1. Baumgartner, T.; Burkart, R.M.; Kolar, J. Analysis and Design of a 300-W 500 000-r/min Slotless Self-Bearing Permanent-Magnet Motor. *IEEE Trans. Ind. Electron.* **2014**, *61*, 4326–4336.
2. Nguyen, Q.D.; Ueno, S. Modeling and control of Salient-Pole Permanent Magnet Axial-Gap Self-Bearing Motor. *IEEE Trans. Mechatron.* **2011**, *16*, 516–528.
3. Qiu, Z.J.; Deng, Z.Q.; Wang, X.L.; Meng, X.L. Study on the Modeling and Control of a Permanent-magnet-type Bearingless Motor Considering Rotor Eccentricity and Lorenz Force. *Proc. Chin. Soc. Electr. Eng.* **2007**, *27*, 64–70.
4. Zhu, H.Q.; Cheng, Q.L.; Wang, C.B. Modeling of bearingless permanent magnet synchronous motor based on mechanical to electrical coordinates transformation. *Sci. China Ser. E* **2009**, *52*, 3736–3744.
5. Ooshima, M.; Miyazawa, S.; Chiba, A.; Nakamura, F.; Fukao, T. A rotor design of a permanent magnet-type bearingless motor considering demagnetization. In Proceedings of the Power Conversation, Nagaoka, Japan, 3–6 August 1997; pp. 655–660.
6. Sun, X.D.; Zhu, H.Q.; Zhang, T. Nonlinear decoupling control for 5 degrees-of-freedom bearingless permanent magnet synchronous motor. In Proceedings of the Power Electronics and Motion Control Conference, Wuhan, China, 17–20 May 2009.
7. Kascak, P.; Jansen, R.; Dever, T.; Loparo, K.; Nahorny, A. Motoring performance of a conical pole-pair separated bearingless electric machine. In *Energyteck*; IEEE: New York, NY, USA, 2011; pp. 1–6.
8. Zhang, S.; Luo, F.L. Direct control of radial displacement for bearingless permanent-magnet-type synchronous motors. *IEEE Trans. Ind. Electron.* **2009**, *56*, 542–552.
9. Sun, X.D.; Zhu, H.Q.; Zhang, T. Sliding mode variable structure control for radial suspension forces of bearingless permanent magnet synchronous motor based on inverse system method. In Proceedings of the Power Electronic and Motion Control Conference, Wuhan, China, 17–20 May 2009.
10. Sun, X.D.; Zhu, H.Q.; Pan, W. Decoupling control of bearingless permanent magnet-type synchronous motor using artificial neural networks-based inverse system method. *Int. J. Model. Ident. Control* **2009**, *8*, 114–121.
11. Khoo, W.K.S. Bridge configured winding for polyphase self-bearing machines. *IEEE Trans. Magn.* **2005**, *41*, 1289–1295.

12. Zhang, S.R.; Luo, F.L. Direct Control of Radial Displacement for Bearingless Permanent-Magnet-Type Synchronous Motors. *IEEE Trans. Ind. Electron.* **2009**, *56*, 542–552.
13. Amrhein, W.; Silber, S.; Nenninger, K. Levitation forces in bearingless permanent magnet motors. *IEEE Trans. Magn.* **1999**, *35*, 4052–4054.
14. Chiba, A.; Fukao, T.; Ichikawa, O.; Oshima, M.; Takemoto, M.; Dorrell, D.G. *Magnetic Bearings and Bearingless Drives*; Elserver: Amsterdam, The Netherland, 2005; p. 400.
15. Chiba, A.; Hanazawa, M.; Fukao, T.; Rahman, M.A. Effects of magnetic saturation on radial suspension force of bearingless synchronous reluctance motors. *IEEE Trans. Ind. Appl.* **1996**, *32*, 354–362.
16. Li, H.; Zhu, H.Q. Bearingless motor's radial suspension force control based on virtual winding current analysis. In Proceedings of the Electrical Machines and Systems (ICEMS), Hangzhou, China, 22–25 October 2014; pp. 2141–2146.
17. Pillay, P.; Krishnan, R. Modeling of permanent magnet motor drives. *IEEE Trans. Ind. Election.* **2002**, *35*, 537–541.
18. Sun, X.D.; Chen, L.; Yang, Z.B.; Zhu, H.Q.; Zuo, W.Q.; Shi, K. Modeling of a Bearingless Permanent Magnet Synchronous Motor Considering Rotor Eccentricity and Coupling Relationship of Windings. *Trans. CES* **2013**, *28*, 63–70.
19. Zhu, H.Q.; Wei, J. Radial suspension force modeling on interior bearingless permanent magnet synchronous motors. *Electr. Mach. Control* **2013**, *5*, 45–50.
20. Zhu, H.Q.; Wu, L.; Li, T.H.; Sun, Y.K. Suspension principle of rotor and decoupling control for bearingless permanent magnet-type synchronous motors. *J. Southeast Univ. (Nat. Sci. Edit.)* **2005**, *35*, 34–38.
21. Inagaki, K.; Chiba, A.; Rahman, M.A.; Fukao, T. Performance characteristics of inset-type permanent magnet bearingless motor drives. In Proceedings of the Power Engineering Society Winter Meeting, Singapore, 23–27 January 2000; pp. 202–207.
22. Deng, Z.Q.; Qiu, Z.J.; Wang, X.L.; Yan, Y.G. Study on rotor flux orientation control of permanent magnet bearingless synchronous motors. *Proc. Chin. Soc. Electr. Eng.* **2005**, *25*, 48–52.
23. Munteanu, G.; Binder, A.; Schneider, T.; Funieru, B. No-load tests of a 40 kW high-speed bearingless permanent magnet synchronous motor. In Proceedings of the 2010 International Symposium on Power Electronics Electrical Drives Automation and Motion (SPEEDAM), Pisa, Italy, 14–16 June 2010; IEEE: New York, NY, USA; pp. 1460–1465.
24. Yajima, S.; Takemoto, M.; Tanaka, Y.; Chiba, A.; Tadashi, F. Total efficiency of a deeply buried permanent magnet type bearingless motor equipped with 2-pole motor windings and 4-pole suspension windings. In Proceedings of the Power Engineering Society General Meeting, Tampa, FL, USA, 24–28 June 2007; IEEE: New York, NY, USA; pp. 1–7.